

Multiobjective optimization in combinatorial wind farms system integration and resistive SFCL using analytical hierarchy process



Amirhasan Moghadasi ^{a,*}, Arif Sarwat ^a, Josep M. Guerrero ^b

^a Energy Systems Research Laboratory, Florida International University, FL, USA

^b Department of Energy Technology, Aalborg University, Aalborg, Denmark

ARTICLE INFO

Article history:

Received 18 June 2015

Received in revised form

17 March 2016

Accepted 21 March 2016

Available online 31 March 2016

Keywords:

Low voltage ride-through

Multi-objective optimization

Superconducting fault current limiter

Wind farm

ABSTRACT

This paper presents a positive approach for low voltage ride-through (LVRT) improvement of the permanent magnet synchronous generator (PMSG) based on a large wind power plant (WPP) of 50 MW. The proposed method utilizes the conventional current control strategy to provide a reactive power requirement and retain the active power production during and after the fault for the grid codes compliance. Besides that, a resistive superconducting fault current limiter (RSFCL) as an additional self-healing support is applied outside the WPP to further increase the rated active power of the installation, thereby enhance the dc-link voltage smoothness, as well as the LVRT capability of the 50 MW WPP. This is achieved by limiting the exceed fault current and diminishing the voltage dip level, leading to increase the voltage safety margin of the LVRT curve. Furthermore, the effect of the installed RSFCL on the extreme load reduction is effectively demonstrated. A large WPP has a complicated structure using several components, and the inclusion of RSFCL composes this layout more problematic for optimal performance of the system. Hence, the most-widely decision-making technique based on the analytic hierarchy process (AHP) is proposed for the optimal design of the combinatorial RSFCL and 50 MW WPP to compute the three-dimensional alignment in Pareto front at the end of the optimization run. The numerical simulations verify effectiveness of the proposed approach, using the Pareto optimality concept.

© 2016 Elsevier Ltd. All rights reserved.

1. Introduction

Wind turbines with the grid connected mode of the operation play the significant role toward in sustainable energy development in the future. However, integration of large wind power plants (WPPs) can impose the adverse effects on the grid, particularly under abnormal grid voltage conditions [1]. Traditionally, wind turbine generators were tripped with circuit breakers once the voltage at their terminals reduced below 80% because the penetration level of the wind power was extremely small compared to the conventional generation systems and their impact on the grid was low. The trend towards integration of more WPPs has raised serious concerns about the stability of existing power networks, increasing the fault current levels and voltage reductions, thereby disconnecting a large wind farm. Recently, many power system operators in Europe and other parts of the world are expanding and

modifying their interconnection requirements for wind farms through technical standards known as grid codes [2–4].

One of the critical demanding requirements, concerning the grid voltage support, is called low voltage ride-through (LVRT) capability, which is regularly being included in the new grid codes. Fig. 1(a) shows practical example of the LVRT curve defined by the Danish system operator for wind turbines (WTs) connected to the grid. Based on this regulation, if the voltage remains at the level greater than 20% of nominal for a period less than 0.5 s, the WT should be connected to the grid. WTs are only stipulated to disconnect from the grid when the voltage profile falls into the Area B. Besides the LVRT requirements, some grid codes require large WTs to contribute to the voltage restoration of the power system by injecting the reactive power during the fault and the recovery period [3], while maintaining the operating point above the area of Fig. 1(b).

Permanent magnet synchronous generators (PMSGs) with a full-rating converter offers a number of advantages for WTs, including low maintenance requirements, more reactive power supply and better ride-through capability because power electronic converters are decoupled completely from the grid [5–7]. However,

* Corresponding author. Office: EC3920, Lab: EC 3920, Florida International University (FIU), 10555 West Flagler St., EC3913, Miami, FL, 33174, USA.

E-mail address: amogh004@fiu.edu (A. Moghadasi).

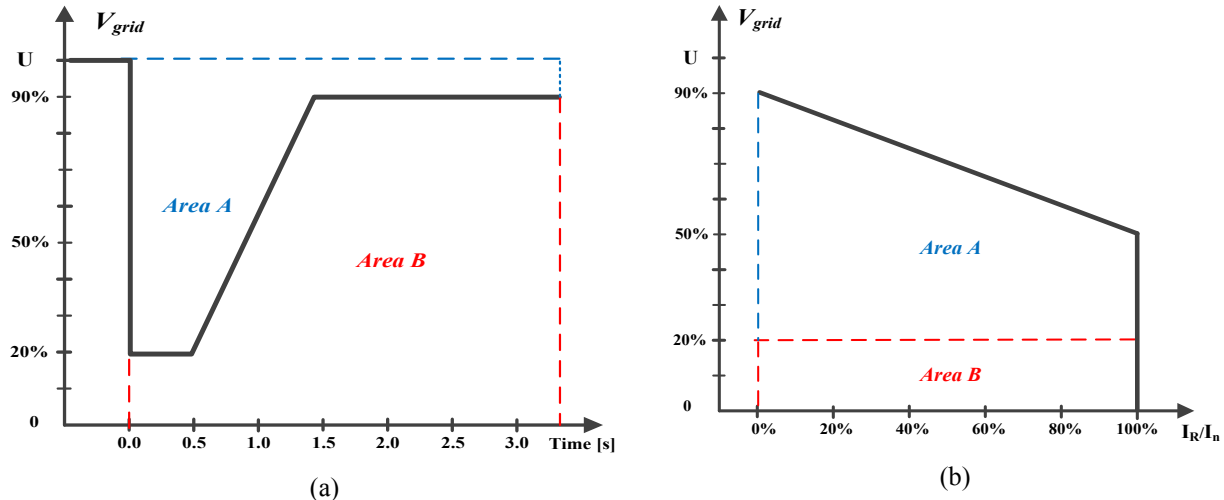


Fig. 1. Danish grid codes. (a) LVRT requirement. (b) Reactive power support requirement.

there is a strong interaction between the turbine control system and the mechanical loads the turbine experiences. The mechanical loads are divided into two distinct types: extreme and fatigue loads. Extreme loads are loads that a given component needs to be able to withstand once; while fatigue loads are accumulating over time and threaten to damage the turbine after several years of operation [8]. An important source of extreme loads may occur during fault events. At the beginning of the fault, the maximum power injected into the grid reduces proportional the voltage sag amplitude, while power injected from the wind generator remains relatively constant. Due to unbalance power between the mechanical-input power and the electrical-output power, the dc-link voltage as well as rotor speed exceeds their safety limits which can potentially force the wind turbine to disconnect from the grid. The quickly growing power ratings of the wind turbines simply exacerbate these problems. Thus, PMSG suffers from large variations of dc-link voltage during and after the grid fault and extreme loads occurring either prior or during the shut-down process [3,8,9]. Any control system that helps to avoid unnecessary faults or that improves the behavior during the shut-down process will reduce turbine loads or contribute to turbine availability.

Several studies have been proposed in the literature to limit the dc-link voltage variations and improve the LVRT capability of PMSG-based wind turbines [5–12]. Fast pitch control can help to reduce the input-mechanical power by rotating the blades about their longitudinal axis, also called pitching, and consequently curbs dc-link voltage fluctuations. In Refs. [13], a logical fast pitch controller along with fuzzy logic controller (FLC) for back to back converters has been proposed in order to enhance the transient performance of WTs during severe network disturbances. Another solution is to permit the excess wind energy to be temporarily stored in the turbine-generation shaft inertia during the grid faults [7,11]. Although, techniques are the cheapest solutions for enhancing the LVRT capability of PMSG-based wind turbines, but these have a very slow dynamic response due to the mechanical constraints of the system, (the speed of the pitch actuator is slow to contribute alone to LVRT support). The most well-known method that is being used for the PMSG-based WT systems is the braking chopper (BC) with the low cost advantage and the simple control performance to consume this surplus power [14,15]. However, in the large wind power plant, including many single wind turbines, the overall cost of using the BCs will be dramatically increased. Moreover, it is difficult to improve the power quality at the output of the wind turbine systems since the BC can just dissipate the

power [16].

Various control methods are also proposed to ensure proper converter operation during fault conditions. The formerly analyzed converter control solutions [11,17,18], are based on the classical approach of using the linear proportional–integral (PI) regulators and pulsewidth/space vector modulation (PWM/SVM). The particular problem is that a linear PI controller is designed for normal network voltage levels, resulting in excessive currents at reduced voltage levels during the fault [10]. The nonlinear control methods are introduced to improve the classical current control method [19,20], but most of these methods are complex and very sensitive to system parameters for practical applications, and need proper tuning of control [21].

This paper proposes an effective approach using resistive superconducting fault current limiter (RSFCL) as the additional support along with conventional converter control strategy based on PI regulators to further increase the rated active power of the installation, thereby enhancing dc-link voltage smoothness as well as the LVRT capability of the 50 MW WPP. By using the RSFCL, the fault current is suppressed effectively and the voltage dip level of the WPP terminals is diminished, leading to enlarge the voltage safety margin of LVRT curve. Up to the present time, as far as the authors are aware, there has been no report on the RSFCL investigation in the large-scale of PMSG-based on WPP, which is the main motivation of this paper.

The first-cycle suppression of a fault current by a RSFCL can also reduce the activation of pitch angle control and can decrease the effect of the extreme loads on the turbine components. A RSFCL is considered as self-healing technology since it eliminates the need for any control action or human intervention due to its automatic excessive current detecting and automatic recovering from non-superconducting to superconducting states [23,24]. These significant features of RSFCL can demonstrate that the proposed technique surpasses aforementioned methods using BCs and complicated nonlinear control system.

However, a large WPP has a complicated structure using several components, and the inclusion of RSFCL composes this scheme more problematic for optimal performance of the system. Hence, the further effort in this paper is centralized on the most-widely decision-making technique based on the analytic hierarchy process (AHP) [25,26], for the optimal performance of the combinatorial RSFCL and 50 MW WPP. The technique creates the Pareto optimality for simultaneously optimizing 3-D alignment that rarely reported the power system literature. Effectiveness of the proposed

approach, using the Pareto optimality concept is verified by the numerical simulations. The optimization technique figures out all the nondominated solutions on the Pareto front at the end of the optimization run.

2. Modeling of the PMSG-Based wind turbine

The structure of the proposed system including a 50-MW PMSG WPP and resistive SFCL is schematically shown in Fig. 2. The constituents of the wind turbine are aerodynamic, mechanical, and electrical parts. The generator are completely decoupled from the grid by power electronic converters (grid-side VSC and generator-side VSC which are connected back-to-back through the common dc-link capacitance). PMSG-based WTs may be represented as a combination of subsystems. The framework shown in Fig. 3 is typically used for modeling purposes, in which the relevant mathematical model has been cited in the several literature [6,7,10], and it is summarily considered here.

2.1. Aerodynamic model

According to the Betz theory, the aerodynamic power generated by the rotor is given by Ref. [6].

$$P_A = \frac{1}{2} \rho \pi R^2 v_{\text{wind}}^3 C_p(\lambda, \beta) \quad (1)$$

where ρ is the air density (kg/m^3), R is the radius of the blade (m), v_{wind} is the free-stream wind speed (m/s), and $C_p(\lambda, \beta)$ is the rotor power coefficient. In the PMSG-based WT, the obtained power depends on C_p , which is a function of both tip speed ratio (TSR) λ and blade pitch angle β , in which the TSR is defined as

$$\lambda = \frac{R \omega_{\text{rotor}}}{v_{\text{wind}}} \quad (2)$$

where ω_{rotor} is the rotational turbine speed. The numerical

approximation of the power coefficient [27] is given by following non-linear equations

$$C_p(\lambda, \beta) = 0.73 \left(\frac{151}{\lambda_t} - 0.58\beta - 0.002\beta^{2.14} - 13.2 \right) e^{-\frac{18.4}{\lambda_t}} \quad (3)$$

$$\lambda_t = \frac{1}{\frac{1}{(\lambda - 0.02\beta)} - \frac{0.003}{(\beta^3 + 1)}} \quad (4)$$

In this paper, the optimal values of power coefficient ($C_{p,\text{opt}}$) and tip speed ratio (λ_{opt}) are 0.45 and 8.32, respectively.

The mechanical torque on the rotor T_{rotor} , which is produced by the blades of wind turbine can be calculated as $P_A/\omega_{\text{rotor}}$. Also, Fig. 4 illustrates the relation between the rotational turbine speed and aerodynamic power of the wind turbine, P_A , for various wind speeds v_{wind} , with the blade pitch angle $\beta = 0^\circ$.

For each wind speed, the maximum power point can be acquired corresponding based on given $C_{p,\text{opt}} = 0.45$ and $\lambda_{\text{opt}} = 8.32$ expressed as [27].

$$P_{\text{max}} = 0.5 \rho \pi R^2 \left(\frac{R \omega_{\text{rotor}}}{8.32} \right)^3 \times 0.45 \quad (5)$$

For an average wind speed of 12 m/s, which is used in this paper, the maximum turbine power output 2 MW and rotational speed 1200 rpm are obtained.

The aerodynamic of wind turbines is controlled by pitch control approaches, which have been developed for large WTs. The blades start to move around cut-in speed 4 m/s, and optimal aerodynamic efficiency is achieved at the wind speed rated about 12 m/s. The extra power obtained from wind speed between 4 and 12 m/s may be smoothly curtailed by spinning the blades using a pitch control to avoid overloading the wind turbine system. Fig. 5 depicts the conventional pitch angle regulator in which the input and output of the model are the rotational turbine speed ω_{rotor} and blade angle β , respectively.

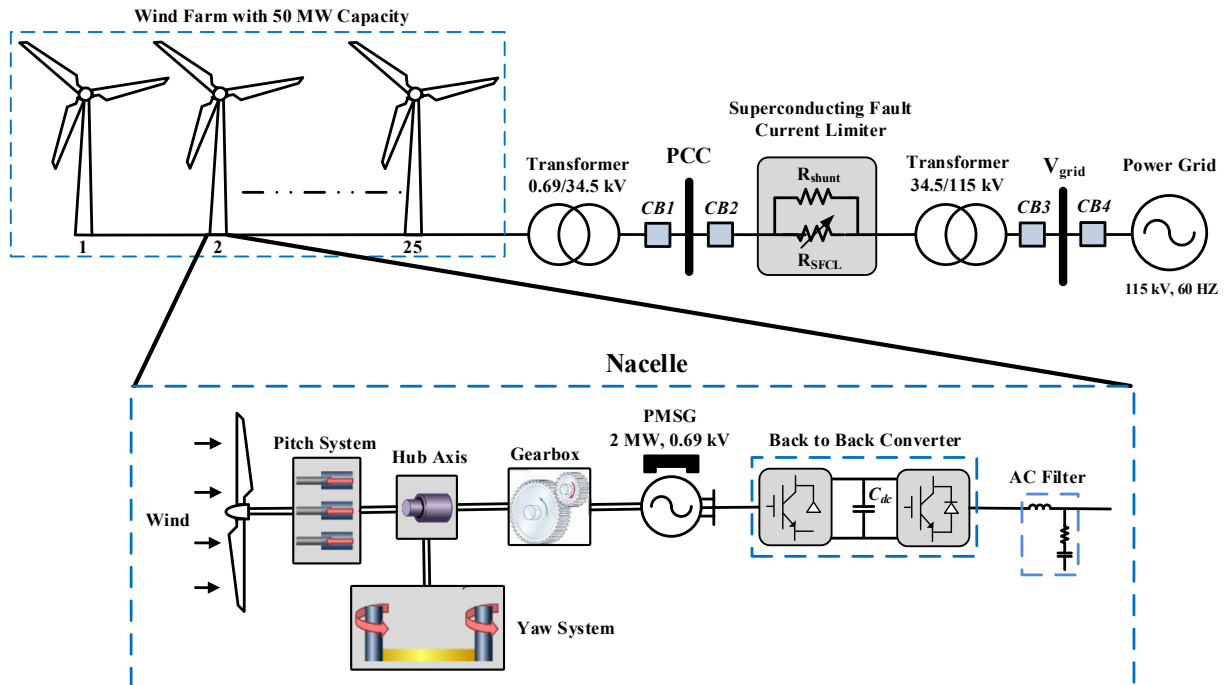


Fig. 2. Proposed combinatorial PMSG-based WPP and RSFCL.

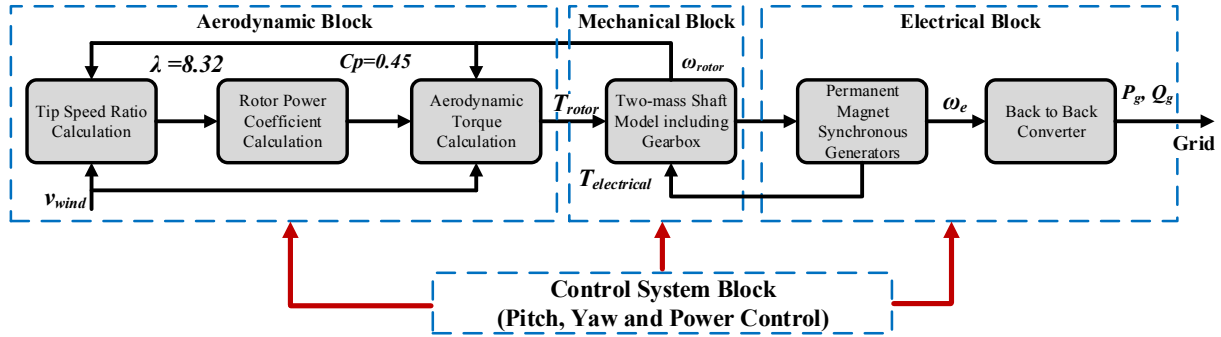


Fig. 3. Subsystems model used in PMSG-based wind turbine.

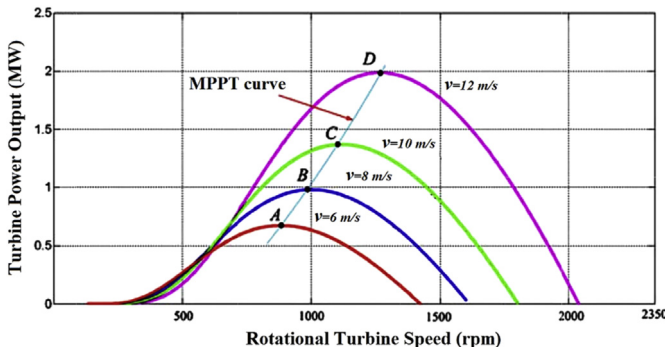


Fig. 4. Wind turbine characteristics.

The yaw system of a typical turbine is significantly slower than the pitch system and the structural dynamics. Since the yaw rates are so slow that there is very little interaction with the rest of the system behavior, it is often not considered at all. If yawing is to be considered it can be modeled similar to the pitch system but with significantly lower bandwidth and rate limits. The gearbox also plays an essential role in the WTs to adapt low-speed, high-torque rotation of the turbine rotor into the faster rotation of the electrical generator. The critical issue in implementing the gearbox technology is the extreme loads, which may lead to misalignment of the drive train and a gradual failure of the gear components, consequently increasing the capital and operating cost of the WTs.

2.2. PMSG model

Based on the reference frame theory [6,11], stator voltage equations in a d-q synchronous frame are modeled:

$$v_{sd} = R_s i_{sd} + L_s \frac{d}{dt} i_{sd} - \omega_e L_d i_{sq} \quad (6)$$

$$v_{sq} = R_s i_{sq} + L_s \frac{d}{dt} i_{sq} + \omega_e L_d i_{sd} + \omega_e \psi_r \quad (7)$$

where v_{sd} and v_{sq} are the d- and q-axes stator voltages, i_{sd} and i_{sq} are

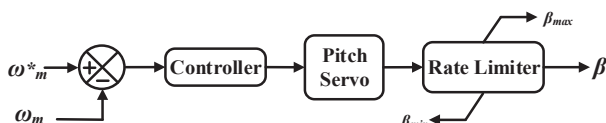


Fig. 5. Conventional pitch angle control used in FSIG-based wind turbine.

the d- and q-axes stator currents, R_s and L_s are the stator resistance and inductance, L_d and L_q are the d- and q-axes inductance, ψ_r is the rotor flux, and ω_e is the electrical angular speed. For the generator with surface-mounted permanent magnets, d- and q-axes inductances are the equal ($L_d = L_q$), resulting a simple interpretation of the electromagnetic torque $T_{electrical}$ and aerodynamic torque on the rotor T_{rotor} expressed as

$$T_{electrical} = \frac{3}{2} p \psi_r i_{sq} \quad (8)$$

$$T_{rotor} - T_{electrical} = J \frac{d}{dt} \omega_{rotor} + b \omega_{rotor} \quad (9)$$

where p is the number of machine pole pairs, J is moment of inertia for turbine-generator, ω_m is shaft mechanical speed, and b is friction coefficient.

3. Power control strategy

Detail of the proposed power control scheme for the PMSG based on the full-power converter topology is illustrated in Fig. 6. As it can be seen, it is schematically divided into two main blocks. On the one hand, controlling the active and reactive power of the PMSG is obtained via a generator-side VSC. On the other hand, the management of the active and reactive power released to the grid by the PMSG along with the dc-link regulation is accomplished via the grid-side VSC. The active and reactive power references to be injected by the grid-side VSC are obtained, so that the whole wind farm can fulfill the grid code requirements.

3.1. Generator-side VSC control

The control block diagram of generator-side VSC is shown in Fig. 6(a), which is based on stator voltage equations (6) and (7) obtained in d-q synchronous frame. Several maximum power point tracking (MPPT) algorithms have been reported for the PMSG-based WT [28–30]. The outcome of the MPPT unit provides the reference value of the rotational turbine speed (ω_m^*) for the generator-side VSC controller. This paper mainly focuses on the converter control, and hence, the MPPT control method was not discussed. The speed reference ω_m^* is acquired by a MPPT method mentioned in (5) in order to extract the maximum amount of power with the actual wind force, while the rotational speed error is given as the input to a PI controller in order to generate the q-axis stator current command (i_{sq}^*). Also, the reactive power produced by the wind turbine is regulated at zero ($i_{sd}^* = 0$) for unity power factor operation. The error between the reference dq-axis currents and the actual dq-axis currents, i_{sd} , i_{sq} are used as inputs to the linear PI

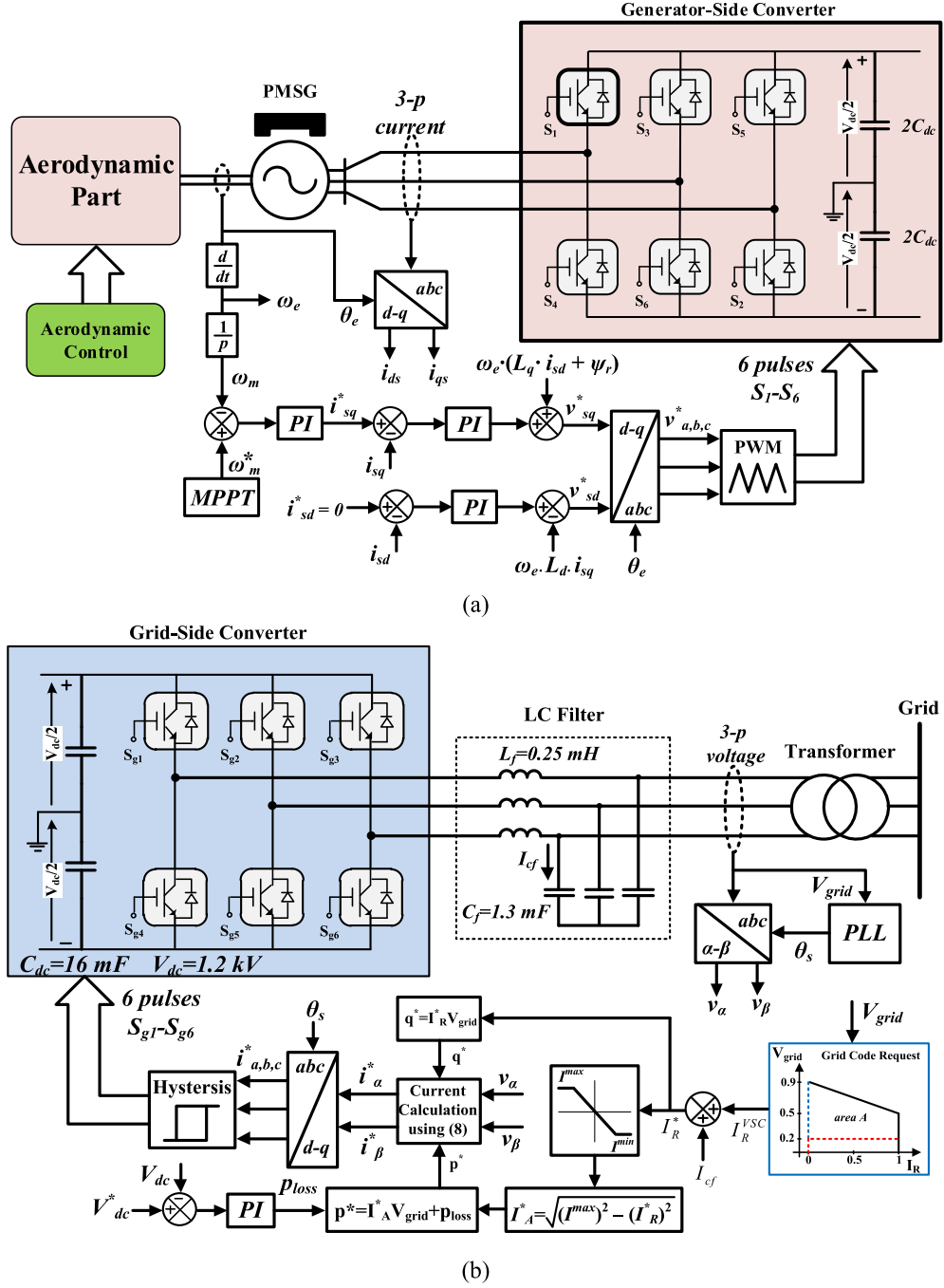


Fig. 6. Proposed power control strategy for WPP. (a) Control block diagram of the generator-side VSC. (b) Control block diagram of the grid-side VSC.

controllers to produce dq-axis voltage commands, v_{sd}^* , v_{sq}^* after the decoupling. The angle θ_e calculated from the rotational speed of the PMSG is applied in a park transformation to engender gate signals using the carrier wave of pulse width modulation (PWM) operation.

3.2. Grid-side VSC control

The proposed grid-side converter controller is provided in Fig. 6(b) to calculate the current references to be inserted by the grid-side VSC in order to fulfill the grid code requirements. Further, this controller preserves the dc-link capacitor voltage at the set value 1.2 kV, which assures the active power swapping from the

PMSG to the grid. In the steady state condition, the maximum capacity of current, I_{max} is used to produce 2 MW active power ($I_R^{VSC} = 0$). In the next stage, p^* , which is added to the PI controller from the dc-link voltage regulator, and q^* transformed into the instantaneous power $\alpha-\beta$ method based on $\alpha-\beta-0$ reference frame [23]. It has been mathematically formulated as

$$\begin{bmatrix} I_\alpha^* \\ I_\beta^* \end{bmatrix} = \frac{1}{v_\alpha^2 + v_\beta^2} \begin{bmatrix} v_\alpha & -v_\beta \\ v_\beta & v_\alpha \end{bmatrix} \begin{bmatrix} p^* + p_{loss} \\ q^* \end{bmatrix} \quad (10)$$

The angle θ_s for the Park transformation is detected from the three-phase voltages at the low-voltage side of the grid transformer by using a phase-locked loop (PLL). Finally, gate signals are

generated for grid side VSC switches using the Hysteresis module [31], shown in Fig. 6(b). Under a grid voltage dip, the reactive current, i_R^{VSC} in proportion to the voltage reduction should be provided during the fault in order to meet the LVRT requirement according to the characteristic shown in Fig. 1(b).

Injection of reactive power has the highest priority in area A, but free capacity of current, I_A^* must also be utilized to retain the active power production related to the voltage sag magnitude, while the generator continues to provide active power at nominal value. In this case, the dc-link voltage exceeds its safety limits, leading a system malfunction or even a component failure. However, the rapidly rising the dc-link voltage, under a system fault, is difficult to be avoided by only using the PI controller. For this reason, this paper proposes a RSFCL used in outside of the wind farm, as shown in Fig. 2. The RSFCL makes it possible to suppress the dc-link voltage fluctuations by limiting the magnitude of the fault current, thereby increasing the output active power capacity and improving the LVRT capability of the wind farm. A further analysis is accomplished in Section 5.

4. Electro-thermal modeling of a RSFCL

The resistive superconducting fault current limiters (RSFCLs) have been launched and introduced into the network as a self-healing technology to curb prospective fault currents immediately to a manageable level by suddenly raising the resistance value [22,23]. Furthermore, after the fault current is profitably repressed, the RSFCL can be restored to the primary state without additional aid. RSFCL has a simple structure with a lengthy superconductor wire inserted in series with the transmission lines. With the recent breakthrough of second-generation high-temperature superconductor (HTS) wires, the SFCL has become more viable [26]. Considering the superconducting material, BSCC-2223 is the conductor, which has commonly been utilized for most of the tentative RSFCLs [32,33].

To preserve the superconductor from detrimental hot spots during the operation, the shunt resistance, R_{shunt} is essential. This parallel resistance must be contacted all over the length of the superconductor, and it regulates the controlled current to elude over-voltages likely occurring when the resistance of the superconductor increases much quicker. The current limiting behavior of the RSFCL can be modeled by the resistance transition of HTS tapes in terms of the temperature and the current density, as defined by the following equation [23].

$$R_{\text{SFCL}} = \left\{ \begin{array}{l} 0, \text{ if } i_{sc} < I_c \text{ and } T < T_c \\ \text{if } i_{sc} > I_c, T < T_c \\ \rho_f \frac{V_{sc}}{A_{sc}^2} \left\{ \frac{J_{c0}}{|J|} \left(\frac{T - T_c}{T_c - T_b} \right) + 1 \right\} \\ \rho_n \frac{V_{sc}}{A_{sc}^2} \left(\frac{T}{T_c} \right), \text{ if } T > T_c \end{array} \right\} \quad (11)$$

where T_c , T_b , J_{c0} , V_{sc} , and A_{sc} are critical temperature, liquid nitrogen temperature, critical current density, superconductor volume, and cross section, respectively. Also, i_{sc} , I_c , ρ_f , and ρ_n are short-circuit current, critical current, flux flow resistivity, and normal resistivity, respectively. In this description (9), three possible states for superconductor are; 1) the flux-creep state at a temperature and a current under the critical rate; 2) the flux flow state at a current over the critical value, but a temperature under the critical rate; and 3) the normal conductive state at a temperature higher the critical amount.

According to the equivalent circuit of the proposed combination,

shown in Fig. 7, if the asymmetrical component of the fault current is ignored, the short-circuit current through the RSFCL branch can be stated by the following equations

$$i_{\text{RSFCL}}(t) = \frac{R_{\text{shunt}}}{R_{\text{SFCL}} + R_{\text{shunt}}} \times \frac{V_m}{\sqrt{R^2 + (L_T \omega)^2}} \sin(\omega t) \quad (12)$$

where $R = R_{\text{trans}} + R_{\text{shunt}}||R_{\text{SFCL}}$, L_T is the inductance of the transformer, and V_m is the magnitude low voltage side of interfacing transformer. The total fault energy dissipated in the HTS tapes, Q_{sc} is calculated using (13), where Δt_{sc} is the duration of the fault [34].

$$Q_{sc-3ph} = 3 \int_{\Delta t_{sc}} R_{\text{SFCL}} i_{\text{RSFCL}}(t)^2 dt \quad (13)$$

Substituting (12) into (13) gives the following

$$Q_{sc-3ph} = \frac{3V_m^2 R_{\text{SFCL}}}{R^2 + (L_T \omega)^2} \left[\frac{\Delta t_{sc}}{2} - \frac{\sin(2\omega\Delta t_{sc})}{4\omega} \right] \quad (14)$$

The RSFCL model should be a reasonable approximation of transient SFCL behavior during faults and, therefore, should consider thermal properties. The thermal model of RSFCL has been generically estimated as follows [24].

$$T(t) = T_0 + \frac{1}{C_{sc}} \int_0^t [Q_{sc}(t) - P_{cool}(t)] dt \quad (15)$$

where T_0 is ambient temperature, C_{sc} is the heat capacity of the superconductor, and P_{cool} is the power cooling.

4.1. Economic feasibility of the RSFCL

Several main factors affect for determining the actual size and the cost of a resistive SFCL, such as the length of applied superconducting wire, the cooling machinery, the geometry of RSFCL module, and the rated power and voltage system, where RSFCL must be installed. Practically, the whole superconducting length is used in form of helix to shape the superconducting tube. In reality, several tubes may be connected in parallel to achieve a particular resistance in form of cylindrical geometry. The rough estimation for the RSFCL size can be achieved based on design details of the RSFCL projects in the worldwide [35]. Accordingly in this paper, the RSFCL module installed in the transmission system with voltage rate of 34.5 kV and power rate of 50 MVA would be much less than 4 m in both diameter and height.

After recent progress of the economical second-generation HTS wires, SFCLs are becoming more practicable, due to low manufacturing costs, low ac losses, higher current densities, and better operational performances, and is eventually expected to be at least a factor of ten lower in the cost than the presently available HTS conductor [36]. The cost of HTS wire is generally described by two parameters: the maximum amount of current that the HTS wire can conduct; and the manufacturing cost per meter of wire.

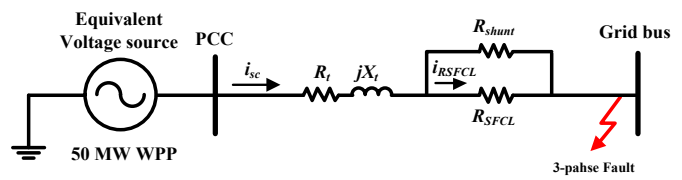


Fig. 7. Equivalent circuit of proposed system in fault condition.

Fig. 8 illustrates how the HTS wire cost of RSFCL is expected to decrease over the next two decades as production increases. The impact of cooling system on the future competitiveness of the RSFCL devices is critical. The 1999 benchmark cost of a medium-sized cryogenic refrigeration unit was about \$60,000/kW_{cold} at 77 K. Economies of scale typical of the cooling refrigeration industry were applied to represent the expected decline in refrigeration costs. This declining cost model indicates that as large numbers of cryogenic refrigeration units are manufactured, the cost will drop to less than \$20,000/kW_{cold} [37].

5. Numerical simulation analysis

The wind farm shown in **Fig. 2** consists of the 25 wind turbines rated at 2 MW, which totally supply the maximum 50 MW to the grid, where the base wind speed is designed as 12 m/s based on ($p_{\omega_{\text{rotor}}}$) characteristic curve (**Fig. 5**). To perform a realistic design, all aspects of a WT need to be considered.

Thus, a holistic wind turbine model was utilized including aerodynamic and mechanical simulations through the FAST software, as well as concurrent electrical simulations through the SimPowerSystems toolbox for MATLAB/Simulink. The FAST aero-elastic wind turbine simulator developed by the National Renewable Energy Laboratory (NREL) to perform detailed simulations of direct-drive and geared wind turbines [38]. The modeling of the RSFCL was also accomplished using MATLAB programming to combine its electrical and thermal properties as discussed in Section 4. A top-level view of the model is shown in **Fig. 9**. The characteristics of the preferred wind farm and selected resistive RSFCL parameters are given in **Appendix A**, **Table 1** and **Table 2**. The simulation results are carried out for the 50 MW system to verify the effective performance of the RSFCL on the dc-link voltage smoothness and the extreme load reduction. All simulations were executed using a fixed-step solver with a 5 μs step size. A three-phase symmetrical grid fault is considered, since the fault ride-through capability of the regional grid codes mostly refer to this type of fault. Thus, a three-phase fault is applied in the middle of the transmission line at $t = 4$ s and is cleared after 200 ms, resulting in a 70% depth of the voltage dip at the PCC. To assess the damping behavior of the RSFCL, simulations are carried out for without and with the presence of the RSFCL. The expediency of the RSFCL component for managing the fault current, as well as resistance and temperature variations of the RSFCL is demonstrated in **Fig. 10**. The peak current for phase a in the pre-fault value is 850 A and then exceeds 14.2 kA without connecting RSFCL, whereas with the RSFCL incorporated on the main road of the wind farm, the fault current is limited effectively to reach about 5.1 kA (see **Fig. 10(a)**).

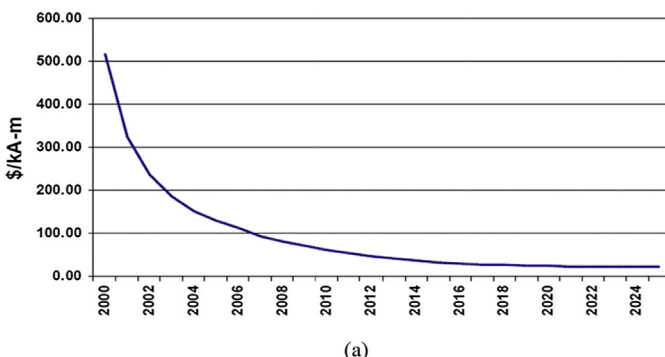
Fig. 10(b) illustrates the limiting resistance of the RSFCL, which

went up to 7.1 Ω in the flux flow state and rise to reach a normal state value of 15 Ω after ten cycles of the fault. A retrieval of **Fig. 10(b)** and (c) will determine, when a fault takes place at $t = 4$ s, the quench time (a transition from a superconducting mode to a resistive mode) is initiated by going through the flux-flow state during of 0.1 s and then to the normal state at a temperature rise of 90 K (critical temperature for HTS tape). **Fig. 11(a)** shows the voltage profile at the PCC in the proposed integration system during a three-phase short circuit. In the absence of the reactive injection and RSFCL, the voltage reduction of 70% occurs. In this case, the voltage at the PCC cannot be restored to the nominal value because of an instability issue on the proposed system and the WPP must be disconnected from the grid. With the adoption of the reactive injection control, the voltage dip is decreased, reaching 50% before recovering immediately to the nominal value upon clearing the fault. Based on the reactive power support requirement (**Fig. 1(b)**), for a 50% voltage reduction, all the capacity of the wind farm is occupied by reactive power.

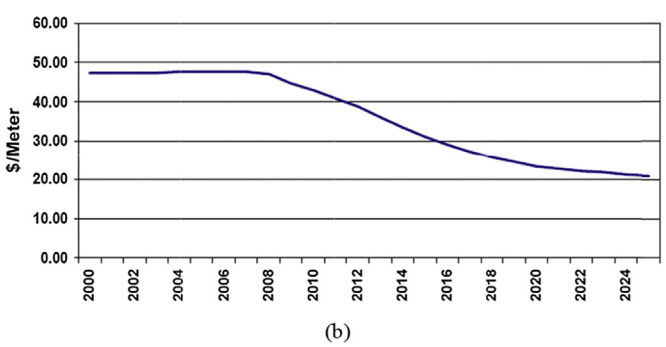
As can be observed in **Fig. 12(b)**, the reactive power injected during the fault (without RSFCL) allows the wind farm to satisfy the specifications of grid code requirements such as increasing the LVRT capacity. However, due to the lack of output active power in the grid-side VSC and consequently the earlier-mentioned unbalanced power during the fault, the dc-link voltage is significantly increased to about 1.14 pu, where a regular reactive power control with no RSFCL is used i.e., 14.58% over voltage (**Fig. 11(b)**). This effort proposes the RSFCL as an additional supporting method besides the reactive power control to improve the LVRT capability and smoothen the dc-link voltage of the wind farm. This method increases the voltage stability margin with respect to the LVRT curve as shown in **Fig. 11(a)**, in which using the RSFCL significantly reduces the magnitude of the voltage sag to around 20%. In addition, the peak value of the dc-link voltage transient is reduced when using the RSFCL, evident by its decline it to 1.05 p.u (less than 5% over voltage), as shown in **Fig. 11(b)**. **Fig. 12(a)** illustrates the active power output of the wind farm with and without the RSFCL, in which it is considerably kept at rated value of 50 MW before occurring the fault. After installing RSFCL, the drop in the active power decreased from 0 MW to 35 MW and back to the normal operation gradually as the fault is cleared. That is, the presence of the RSFCL increases the retaining of the active power production for the PMSG-WPP by approximately 60%, during the fault condition.

5.1. Effect of RSFCL on extreme load reduction on WT structure

In order to analyze the impact of the RSFCL on WT extreme loads, a combination of the FAST model and SimPowerSystems can accurately simulate detailed aerodynamics and mechanical aspects



(a)

**Fig. 8.** HTS wire cost [35]. (a) Dollar per Kiloamp per Meter. (b) Dollar per Meter.

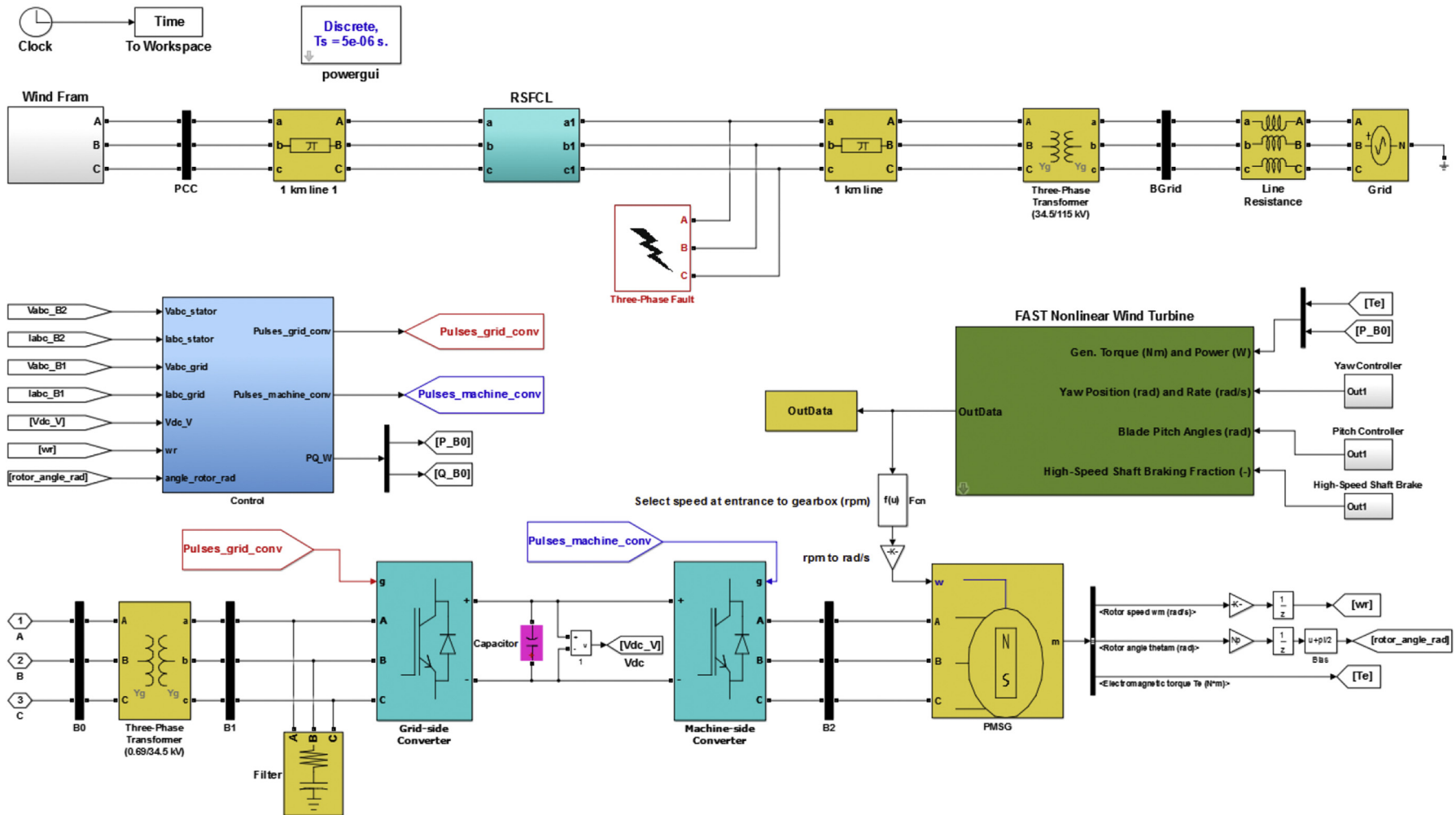


Fig. 9. Combinatorial PMSG-based WT and RSFCL model using FAST aeroelastic simulator and the SimPowerSystems.

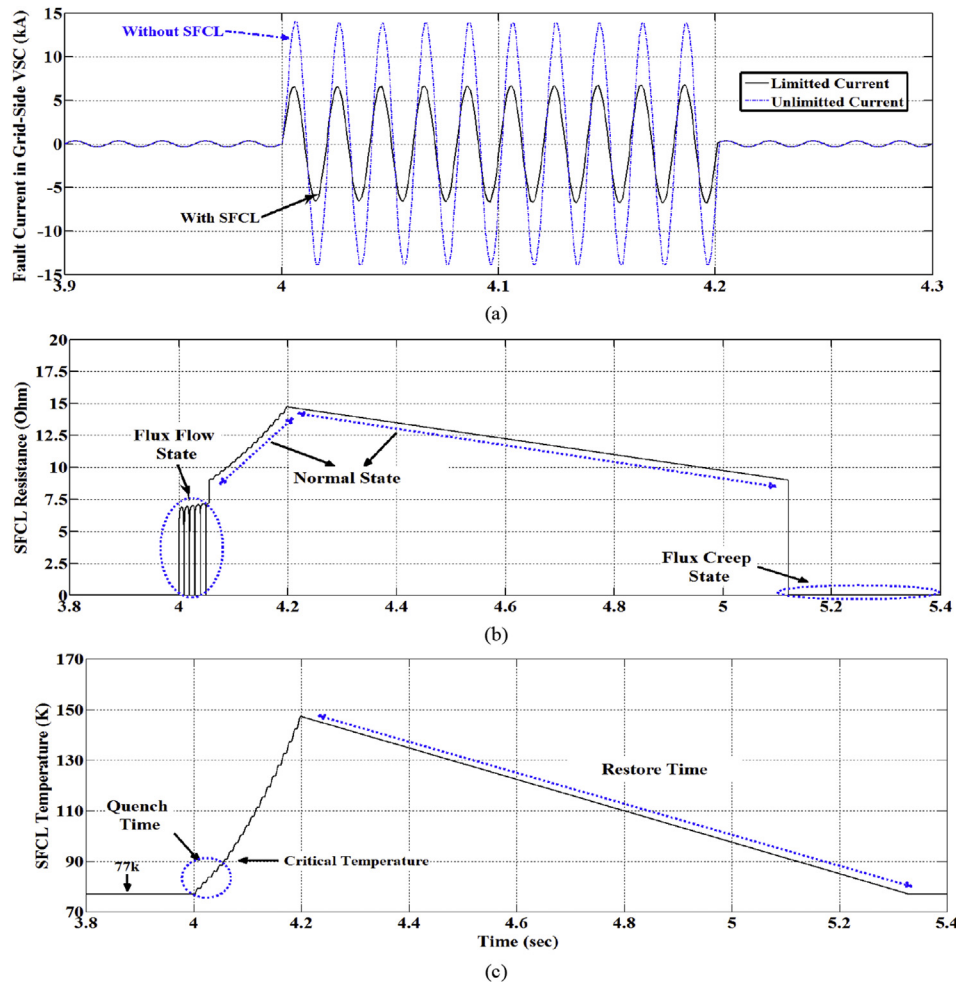


Fig. 10. RSFCL model response. (a) Fault current waveform without and with RSFCL in a single-phase system. (b) Resistance variation in flux flow and normal state. (c) Temperature rise.

of the wind turbine. In this study, it is assumed that wind speed at the hub remains constant at 12 m/s. Rotational speed and mechanical torque responses of the rotor turbine and generator are shown in Figs. 13 and 14, respectively. As it can be seen, the rotational speeds and mechanical torque increase during the fault period, which may lead to power system instability and is detrimental for the turbine generator system if the fault duration is long and proper auxiliary devices are not used (no controller). However, RSFCL can limit the rate of rising of machine speed and the aerodynamic torque imposed on rotor/shaft in order to make better stability.

In this work, a number of the degrees of freedom available in the simulation model are used for analysis of the extreme loads, including tower fore-aft and sideways modes, tower yaw mode, and blade flap wise and edgewise modes [39,40]. All these modes are depicted in Fig. 15, which contains illustrations of a wind turbine seen from the front and side views. The failure at the system causes extreme loads on structural parts of the WTs. Figs. 16–18 show the simulation results of several key loadings, such as hub loadings, blade root loadings, and tower base loadings, of the proposed WPP, which are compared without and with the presence of the RSFCL.

Fig. 16 depicts hub loadings, including the pitch actuator force and yaw moments, during the three-phase fault. The impact of the installed RSFCL on yaw moments is effectively demonstrated by 20% reduction in the magnitude of the value during the fault in

proportion to the case with no using RSFCL, as shown in Fig. 16(a). With the onset of the fault, the pitch actuator force first shows a dip then a rise, and then it reduces to a negative value and finally increases to zero and becomes constant. Rise in the pitch actuator force after it reached negative value is due to large inertia of the rotor. However, application of RSFCL shows a promising solution for reducing the fluctuation of the pitch actuator force, as illustrated in Fig. 16(b).

During the fault, blade experiences moments in flapwise bending and edgewise bending in the blade root. Fig. 17(a) shows the average flapwise bending moment in the blade root. The axial wind force, gravity force and centrifugal force contributes the most to the flapwise bending moment in the blade root. However, the average value of the flapwise moment is almost zero in normal operating state of the WT. At the beginning of the fault, the rotor speed increases, therefore the contribution of centrifugal force in flapwise bending moment in the blade root also increases. As the failure clear quickly after 200 ms, the flapwise moment fluctuations in the blade root gradually smooth, because the contribution because the axial aerodynamic force on rotor becomes negligible. Fig. 17(b) shows the average edgewise bending moment in the blade root. The rotor torque also causes edgewise moment in the blade root and its contribution is estimated by the average value of the edgewise moment. As can be seen, there are several fluctuation trends in the value of the edgewise moment. After clearing the fault, fluctuations trend to fade off fast in edgewise bending

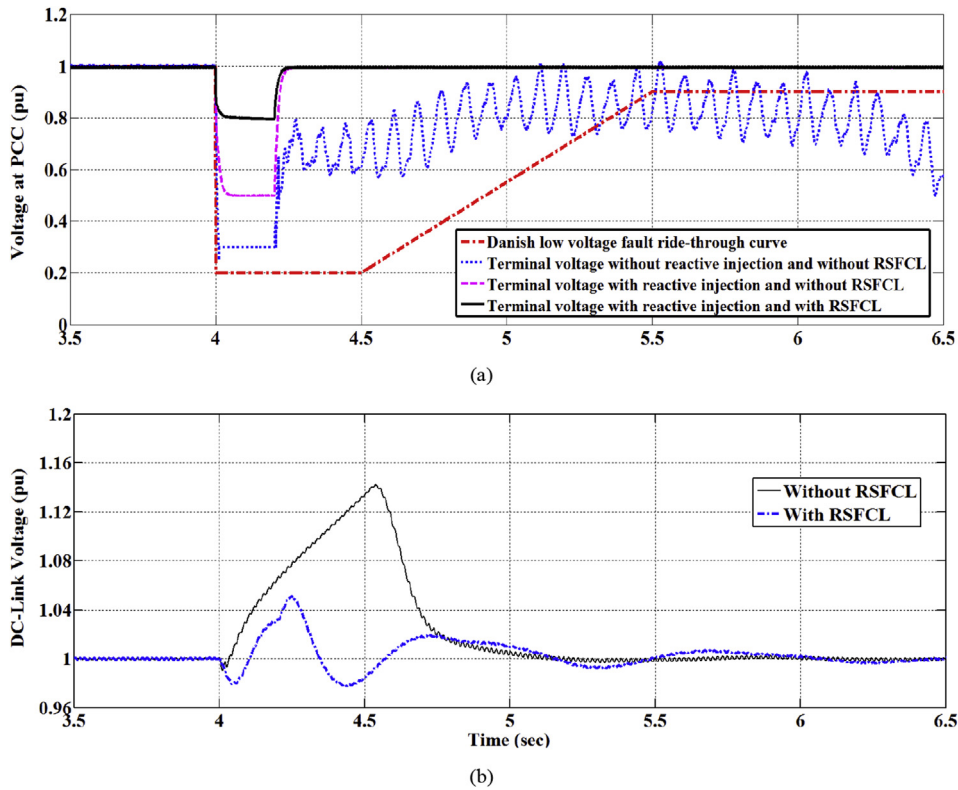


Fig. 11. Operation of the proposed combinatorial WPP and RSFCL during and after fault (a) Voltage profile at wind farm terminal (b) dc-link voltage with and without RSFCL.

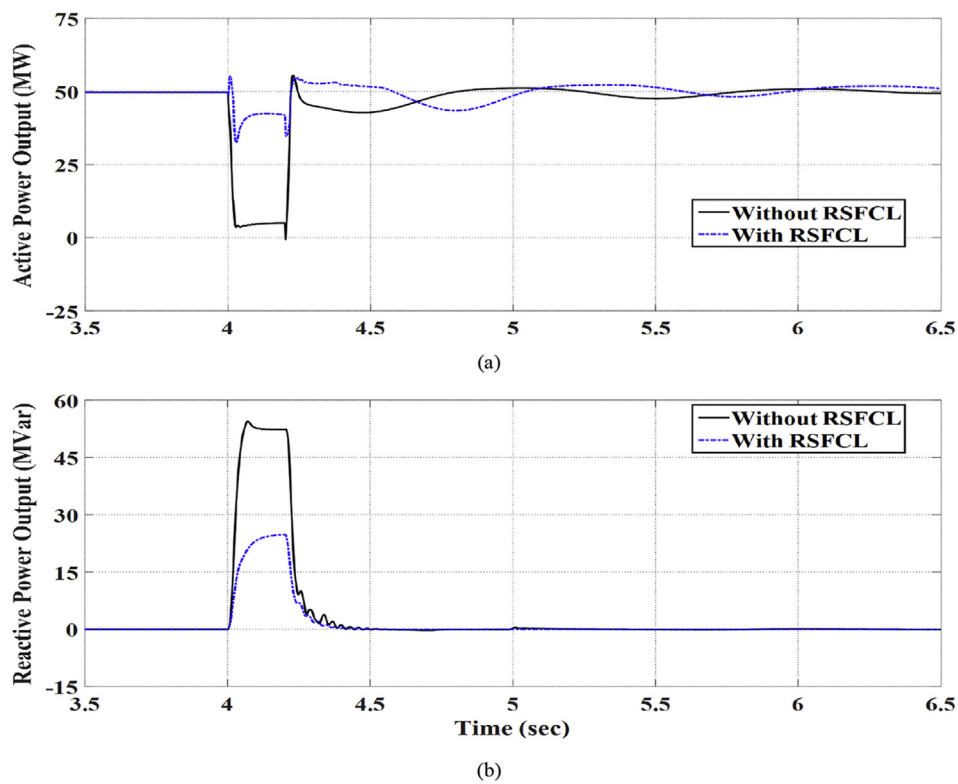


Fig. 12. Operation of the proposed combinatorial WPP and RSFCL during and after fault (a) Active and reactive power at the PCC without the RSFCL. (b) Active and reactive power at the PCC with the RSFCL.

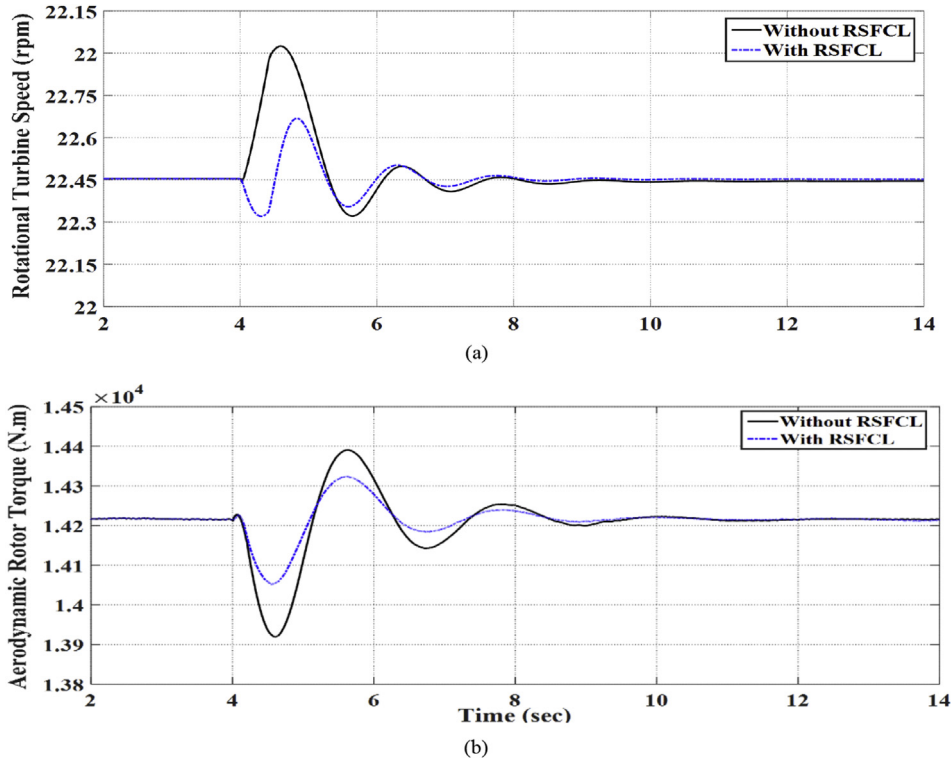


Fig. 13. Dynamic performance of the turbine side with and without applying the RSFCL. (a) Rotational turbine speed. (b) Aerodynamic rotor torque.

moment in the blade root due to the large stiffness in edgewise direction of the blade. In both figures, RSFCL can significantly

dampen the oscillations of the flapwise moment and edgewise moment.

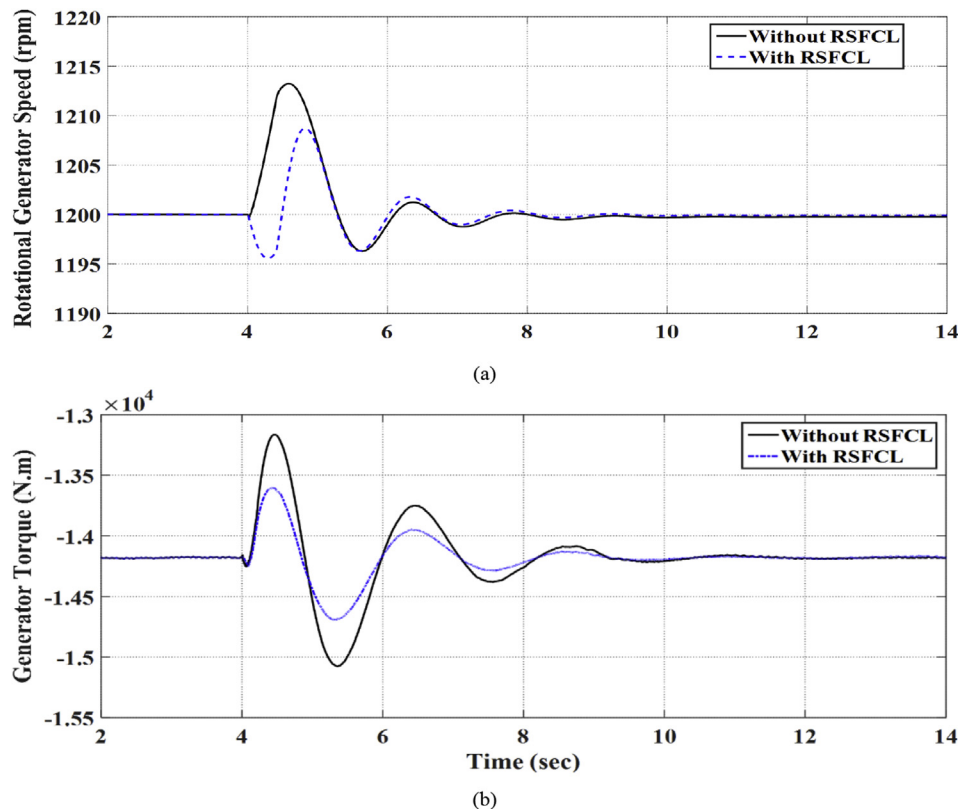


Fig. 14. Dynamic performance of the generator side with and without applying the RSFCL. (a) Rotational generator speed. (b) Generator torque.

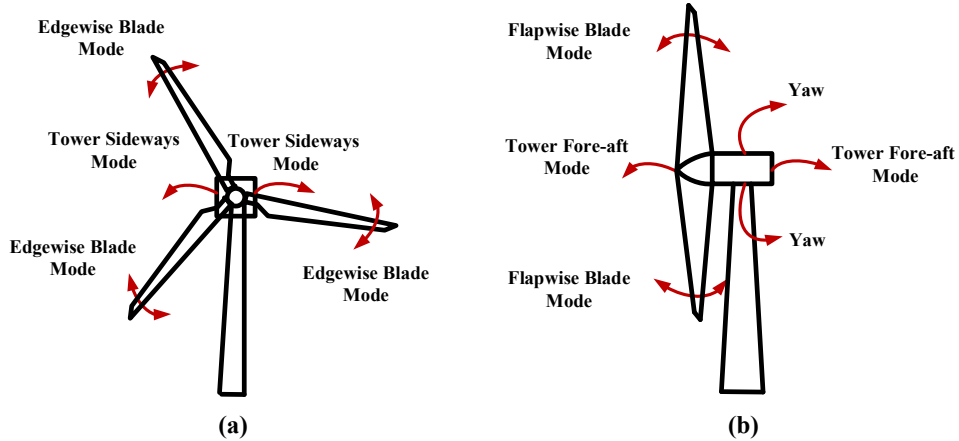


Fig. 15. Wind turbine structure. (a) Wind turbine from the front, illustrating sideways and blade edgewise modes. (b) Wind turbine from the side, illustrating fore-aft, blade flapwise, and yaw modes.

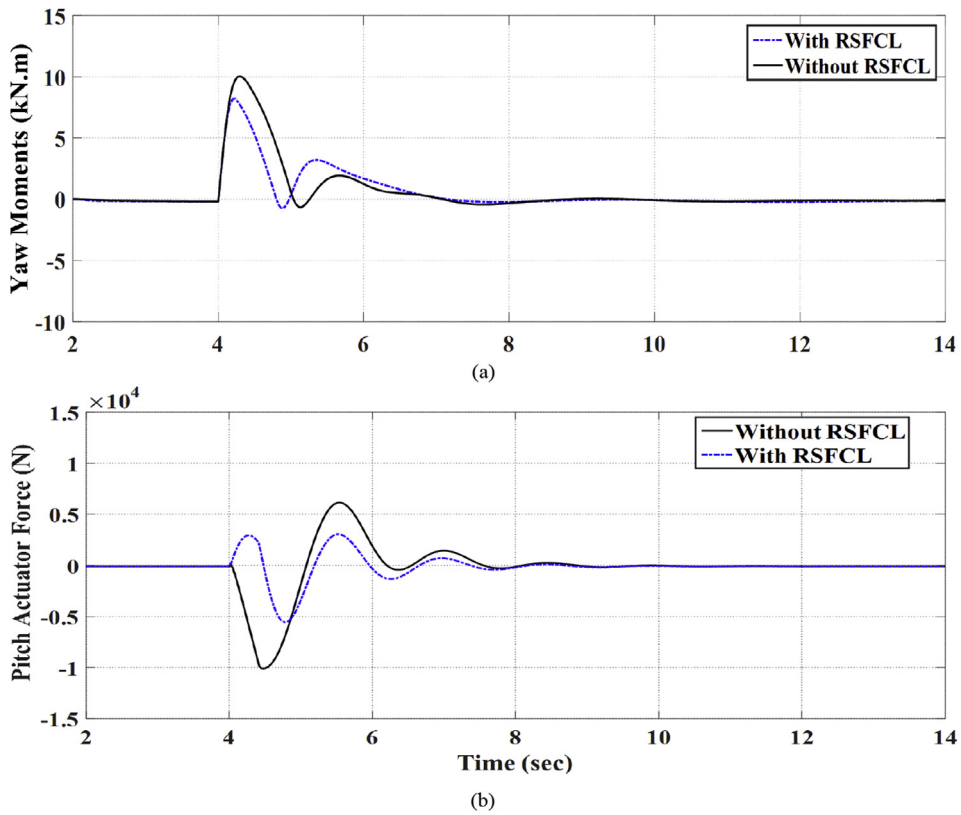


Fig. 16. Dynamic performance of the WT under the extreme load with and without the RSFCL. (a) Yaw moments. (b) Pitch Actuator Force.

The WT tower experiences fore-aft and side-to-side bending moment at the tower base, as shown in Fig. 18. Fore-aft bending moment is mainly due to rotor thrust loading. Tower motions happen due to the tower's dynamic interaction with rotor blades. Due to large fluctuations in axial aerodynamic force on rotor, the tower fore-aft moment also fluctuates.

Once a fault happens in the system, the value of the tower fore-aft moment first increases and then decreases due to the inertia of the tower, as shown in Fig. 18(a).

The tower fore-aft moment first decreases and then increases because of the inertia of tower. The tower fore-aft motion is unable to quickly dampen because the complete weight of the WT operates

on the tower base. Fig. 18(b) shows the side-to-side bending moment in the tower base. The rotor torque that operates on the tower top through gearbox/generator support can lead to the side-to-side tower moment at the tower base. Because of the large inertia of tower, the tower shows fluctuations on the value of the side-to-side moment after clearing the fault, as can be seen in Fig. 18(b).

The results indicate that the proposed RSFCL has significant effect for reducing the fluctuations on the, blade flapwise add edgewise moments, pitch actuator force and yaw moments, and tower fore-aft and side-to-side moments. Therefore, RSFCL can be a promising solution for wind turbine controller performance with

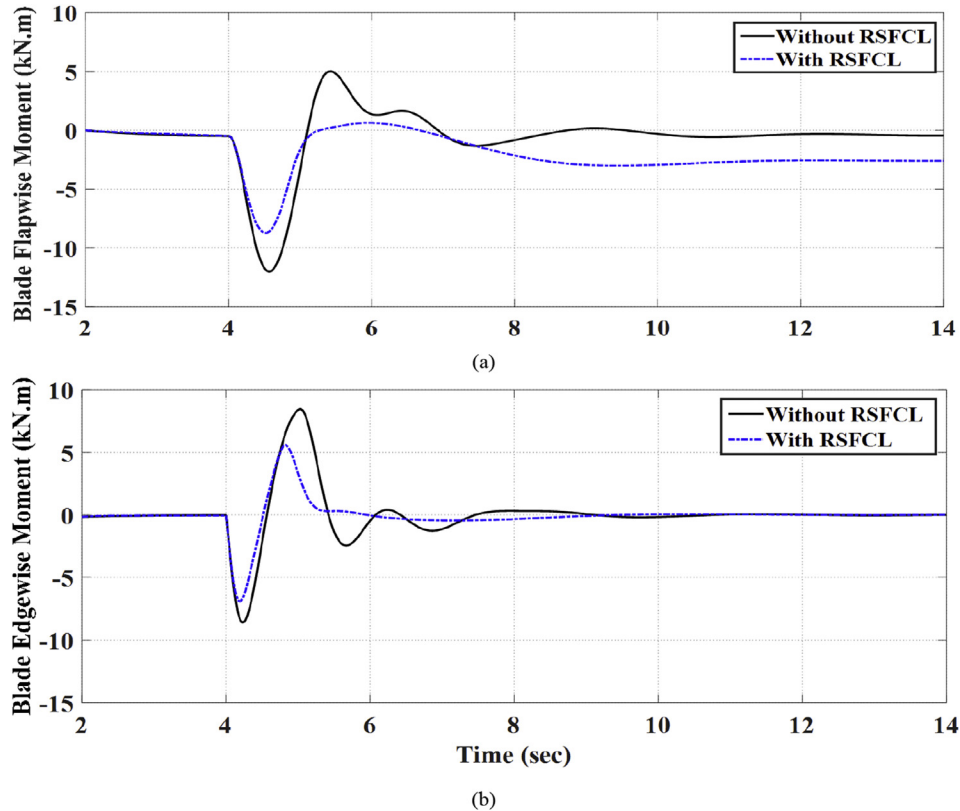


Fig. 17. Dynamic performance of the WT under the extreme load with and without the RSFCL. (a) Blade flapwise moment. (b) Blade edgewise moment.

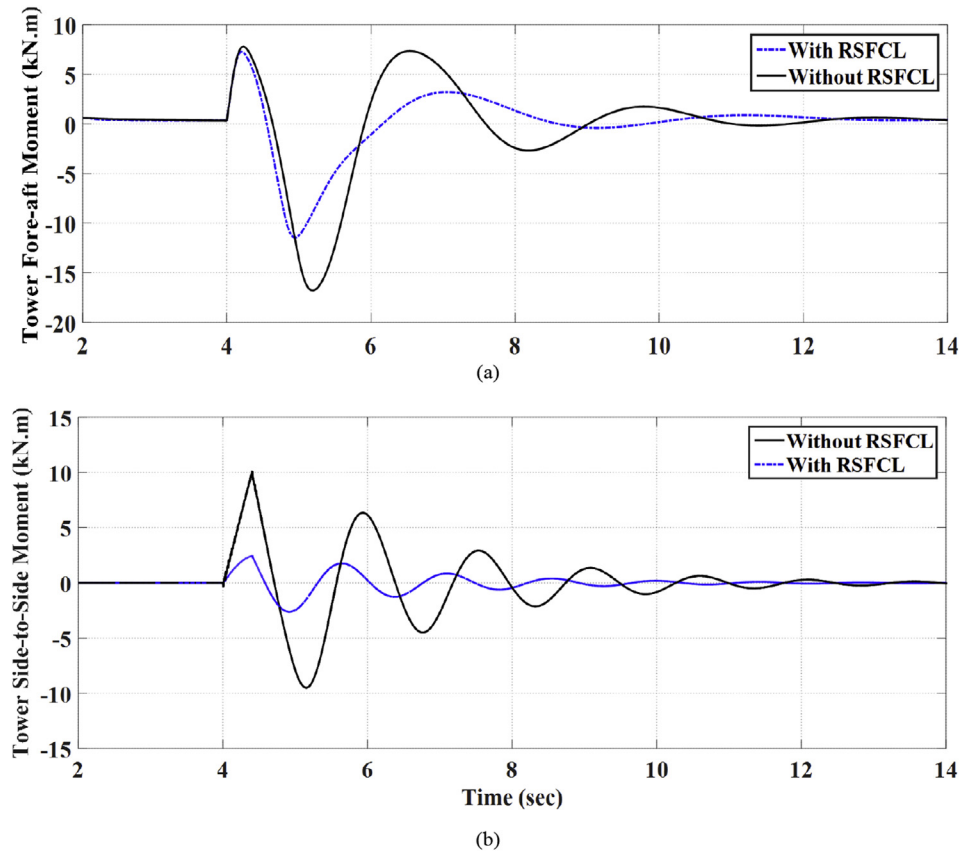


Fig. 18. Dynamic performance of the WT under the extreme load with and without the RSFCL. (a) Tower fore-aft moment. (b) Tower side-to-side moment.

respect to extreme loads happening to mechanical and aerodynamic parts during the severe disturbances.

6. Optimal scheme performance

The obtained results in Section 5 for the proposed combinatorial 50-MW wind farm and RSFCL confirmed that further improvements in dc-link smoothness, extreme load, and LVRT capability of a wind farm can be achieved by increasing the SFCL resistance as much as possible. However, as stated in (14), the high-resistance SFCL means a substantial amount of energy is dissipated in the form of heat, resulting damage on SFCL construction and cooling system. This large energy dissipation would lengthen the recovery time of the RSFCL (transition from resistive state to superconducting state) after clearing the fault. Also, as stated in Section 3.2, for overcoming the unbalance power between the generator and converter, the active power output of the wind farm, P_{WPP} should be appropriately increased during the fault to diminish the fluctuations of dc-link capacitor voltage. However, depending on the grid code, reactive power production has highest priority during the fault, occupying some portion of the maximum capacity of apparent power, and leading reduction in P_{WPP} . Hence, there is a tradeoff between three above mutually contradicting criteria, SFCL resistance, energy dissipation, and active power output of the WPP in order to achieve an optimal design of combinatorial 50-MW wind farm and resistive SFCL.

For optimization purposes, this section implements multi-criteria decision making (MCDM) methodology based on analytical hierarchy process (AHP) detailed in the authors' prior work [23]. One of the outstanding characteristics of the MCDM technique is the creation of the Pareto optimality for simultaneous multi-objective optimization in which algorithm figures out all the non-dominated solutions on the Pareto front (optimality) at the end of the optimization run. AHP is established as beneficial technique providing the promising solutions to the complicated decision-making problems with different criteria. The proposed optimization model contains three predefined criteria and two constraints that are expressed as:

$$\begin{aligned} \text{Min} & \left\{ \frac{1}{R_{SFCL}}, \frac{1}{P_{WPP}}, Q_{SC} \right\} \\ \text{Subject to} & \left\{ \begin{array}{l} T_{SFCL}^{\max} - 423 < 0 \\ \text{point } (V_{grid}, \Delta t_{sc}) \text{ within Area } A \end{array} \right. \end{aligned} \quad (16)$$

$$[C]_{3 \times 3} = \begin{matrix} C_1 & C_2 & C_3 \\ C_1(R_{SFCL}) & \begin{bmatrix} c_{11} & c_{12} & c_{13} \\ c_{21} & c_{22} & c_{23} \\ c_{31} & c_{32} & c_{33} \end{bmatrix} & \begin{bmatrix} C_1/C_1 & C_1/C_2 & C_1/C_3 \\ C_2/C_1 & C_2/C_1 & C_2/C_3 \\ C_3/C_1 & C_3/C_2 & C_3/C_3 \end{bmatrix} \\ C_2(P_{WPP}) & & \\ C_3(Q_{SC}) & & \end{matrix} = \begin{bmatrix} 1 & 9/5 & 9 \\ 5/9 & 1 & 5 \\ 1/9 & 1/5 & 1 \end{bmatrix} \quad (17)$$

Where, maximum SFCL appeared resistance, R_{SFCL} maximum active power output of the WPP, P_{WPP} and minimum energy dissipation, Q_{SC} are desirable. The proposed system (combination of 50 MW WPP and RSFCL) should be designed in such a way that the following criteria are satisfied: 1) $T_{SFCL}^{\max} < 432^\circ$ for safe solder melting; and 2) fulfill Danish grid code requirement including LVRT and reactive power support requirement.

Based on (11), any change in the dimensions of the

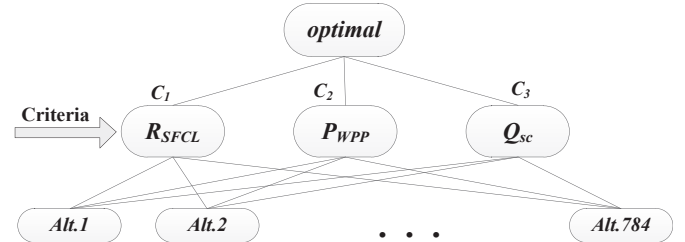


Fig. 19. Hierarchy process for optimal combinatory PMSG-based WT and RSFCL.

superconducting wires as well as fault durations may affect fault current limiting performance of RSFCL, and consequently the optimum design of the proposed system. Therefore, in this optimization, variable parameters are superconducting wire volume (V_{SC}), superconducting wire cross section (A_{SC}) and duration of the fault (Δt_{SC}). The constraints of the selected variables for the optimization problem are shown in Appendix (Table 3).

Considerately, if each variable is changed in 10 steps, three variables would create $10^3 = 1000$ alternatives when utilized in the electrical simulation model. These cases (378) that exceed the predefined optimization constraints must be omitted from feasible options.

The goal of AHP method is to find a best case (desired solution) among the remnant number of 784 alternatives that can maximize each criterion satisfaction. Basically, for 784 alternatives ($A_i, i = 1, 2, \dots, 784$) and 3 criteria ($C_j, j = 1, 2, 3$), there are four steps considering decision problems by AHP as follows:

Step 1) Scrutinize the relation between objectives, criteria and alternatives to build the multi-layers hierarchical structure. Fig. 19 shows the multi-layers hierarchical structure for optimal combinatorial PMSG-based WT and RSFCL including optimal layer, criterion layer, and alternative layer.

Step 2) Compose a pairwise comparison matrix by assigning each alternative/criterion an optional number from 1/9 to 9. In this article, the three-point performance rating scale is defined for the importance of criteria, 9 (high), 5 (medium), and 1 (low). Based on the explanation in Refs. [23], if the importance of criteria C_1, C_2, C_3 are ranked as high ($C_1 = 9$), medium ($C_2 = 5$), and low ($C_3 = 1$), respectively, the criteria pairwise comparison matrix $C = [c]_{3 \times 3}$ can be expressed by

A similar method is applied to estimate the value of alternative pairwise comparison matrix $A_i = [a_{ij}]_{784 \times 784}$ ($i = 1, 2, 3$) with respect to each criterion.

Step 3) Compute the relative weight (priority) of the compared factor for the criterion according to the judgment matrix C and A . The criteria and alternatives weight vectors can be obtained by adding the array elements of each row of C and A matrix and then dividing by the sum of the element of columns. Here, the weight vector matrix of criteria w_{cj} ($j = 1, 2, 3$) can be estimated by

Table 4

Achieved optimal alternatives using AHP method.

Case no.	Priority	w_{c1}	w_{c2}	w_{c3}	$V_{SC} (m^3)$	$A_{SC} (m^2)$	$\Delta t_{sc} (s)$	$R_{SFCL} (\Omega)$	$P_{PMSG} (MW)$	$Q_{SC} (kJ)$
1	H-H-H	0.33	0.33	0.33	5.00E-04	9.20E-07	0.26	44.59	41.35	143.43
2	H-H-M	0.39	0.39	0.22	4.30E-04	1.04E-06	0.32	29.54	44.75	200.95
3	H-H-L	0.47	0.47	0.05	1.85E-04	1.04E-06	0.38	12.72	25.53	252.17
4	H-M-H	0.39	0.22	0.39	4.65E-04	1.04E-06	0.38	31.94	40.94	234.51
5	H-M-M	0.47	0.26	0.26	1.85E-04	9.20E-07	0.44	26.23	32.19	252.17
6	H-M-L	0.60	0.33	0.07	1.85E-04	1.04E-06	0.44	19.72	20.82	291.99
7	H-L-H	0.47	0.05	0.47	3.60E-04	9.20E-07	0.8	31.63	41.71	492.73
8	H-L-M	0.60	0.07	0.33	3.25E-04	9.20E-07	0.74	27.53	31.31	466.48
9	H-L-L	0.82	0.09	0.09	2.90E-04	1.28E-06	0.68	26.15	16.35	448.68
10	M-H-H	0.22	0.39	0.39	3.95E-04	9.20E-07	0.26	34.67	43.42	155.92
11	M-H-M	0.26	0.47	0.26	3.60E-04	1.04E-06	0.26	24.73	38.92	168.14
12	M-H-L	0.33	0.60	0.07	5.00E-04	1.40E-06	0.32	18.95	23.22	211.95
13	M-M-H	0.26	0.26	0.47	2.55E-04	1.04E-06	0.38	17.51	40.74	252.17
14	M-M-L	0.45	0.45	0.09	3.25E-04	1.52E-06	0.5	10.45	29.36	331.38
15	M-L-H	0.33	0.07	0.60	2.90E-04	1.16E-06	0.62	16.01	29.72	409.45
16	M-L-M	0.45	0.09	0.45	3.60E-04	1.52E-06	0.68	11.57	25.89	448.68
17	M-L-L	0.71	0.14	0.14	5.00E-04	1.88E-06	0.62	10.51	18.26	409.45
18	L-H-H	0.05	0.47	0.47	4.30E-04	1.76E-06	0.2	10.31	39.31	131.39
19	L-H-M	0.07	0.60	0.33	2.20E-04	1.64E-06	0.2	7.07	22.31	131.39
20	L-H-L	0.09	0.82	0.09	1.50E-04	1.16E-06	0.26	8.28	28.59	231.62
21	L-M-H	0.07	0.33	0.60	4.30E-04	1.88E-06	0.32	9.04	34.76	211.97
22	L-M-M	0.09	0.45	0.45	2.90E-04	1.64E-06	0.38	8.01	25.25	252.17
23	L-M-L	0.14	0.71	0.14	2.90E-04	1.76E-06	0.38	6.95	20.37	252.17
24	L-L-H	0.09	0.09	0.82	5.00E-04	1.88E-06	0.74	10.51	30.22	128.92
25	L-L-M	0.14	0.14	0.71	3.95E-04	1.76E-06	0.62	9.47	25.96	207.13

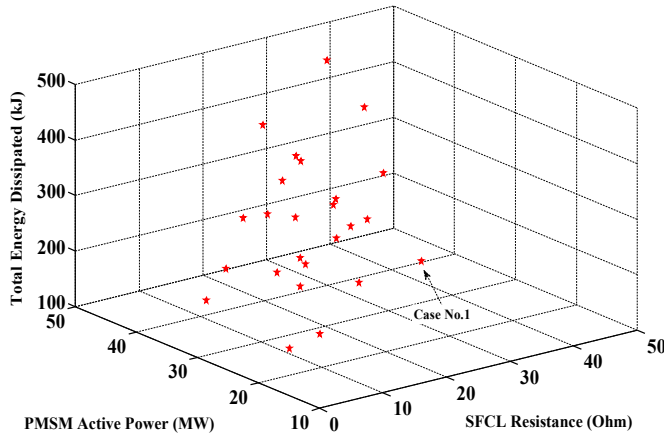


Fig. 20. Multi-objective optimization using AHP, Pareto front for three criteria.

$$\begin{bmatrix} w_{c1} \\ w_{c2} \\ w_{c3} \end{bmatrix} = \frac{1}{(1 + 9/5 + 9) + (5/9 + 1 + 5) + (1/9 + 1/5 + 1)} \begin{bmatrix} 1 + (9/5) + 9 \\ (5/9) + 1 + 5 \\ (1/9) + (1/5) + 1 \end{bmatrix} = \begin{bmatrix} 0.60 \\ 0.334 \\ 0.066 \end{bmatrix} \quad (18)$$

The analysis of the simulation results represents the degree of importance of alternative i in criterion j , i.e., d_{ij} , which is divided by its maximum value. This is followed by splitting the alternation range to 9 parts, allocating a proportional number from 1 to 9 into each alternative a_{ij} as

$$a_{ij} = \text{Integer} \left(\frac{d_{ij}}{0.11 \max_i(d_{ij})} \right) \quad (19)$$

Since, a pairwise comparison matrix of the alternative A_i is compatible; it forms the calculation of the alternative weight vector

simple via normalizing the elements of each column, reaching to wa_{ij} . These calculations can be formulated as

$$wa_{ij} = \frac{a_{ij}}{\sum_{l=1}^{784} a_{lj}} \quad (20)$$

The sum of the entire alternative weight vector with respect to the each criteria wa_{ij} and the criteria weight vector w_{cj} for $j = 1, 2, 3$ & $i = 1, 2, \dots, 784$, forms a decision matrix (784×3) as.

Alts.	Criteria		
	C_1 (w_{c1})	C_2 (w_{c2})	C_3 (w_{c3})
A_1	wa_{11}	wa_{12}	wa_{13}
A_2	wa_{21}	wa_{22}	wa_{23}
\vdots	\vdots	\vdots	\vdots
A_{784}	$wa_{(784)1}$	$wa_{(784)2}$	$wa_{(784)3}$

Step 4) Calculate the best alternative, i.e., the highest priority value.

Usually, the criteria can be classified into the two opposite groups called the benefit and cost criteria [41]. A benefit criterion means that the better alternative has the higher grade. The inverse scenario is expressed true for the cost criteria. In this optimization study, the total energy dissipated is cost and the other criteria, i.e., the resistance of SFCL and power output of the PMSG, are benefit. Thus, the optimization problem can be summarized as a standard format for aggregating alternatives to rank them based on the ratio performance approach detailed in Refs. [37], as given by

$$P_{\text{AHP}}^* = \max_i \left(\frac{(wa_{i1} \times w_{c1}) + (wa_{i2} \times w_{c2})}{wa_{i3} \times w_{c3}} \right) \text{ for } i = 1, 2, \dots, 784 \quad (21)$$

For three levels criteria comparison, this weight vector must be calculated 25 times ($3^3 - 2$) by changing the importance of the criteria with respect to each other. The run results of the algorithm

are shown in **Table 4**. As earlier mentioned, the Pareto optimality plays the significant role in choosing the best solution for optimization of all three criteria: resistance of SFCL, energy dissipation in SFCL, and active power output of the WT. However, for an approximate set of three-dimensional Pareto-optimal solutions, a search is performed for the tradeoff values between the optimums of the objective functions, using AHP, at the end of each optimization run, as shown in **Fig. 20**.

The corresponding AHP optimization results are illustrated in **Table 4**. It is the tradeoff values between the 25 given set of mutually contradicting criteria. Referring to **Table 4**, if higher priority is given to the RSFCL, so case 9 (H-L-L) in which $26.15\ \Omega$ must be chosen. Similarly, for the power output of the PMSG-WPP or total energy dissipated priority selection, cases 20 and 24 (L-H-L and L-L-H) in which $P_{PMSG} = 28.59\text{ MW}$ and $Q_{sc} = 128.92\text{ kJ}$ must be selected, respectively. Moreover, the higher and lower active power delivered during the fault are obtained in case 1 (82.7% of total capacity) and case 9 (32.7%), respectively.

7. Conclusion

The paper proposes an effective approach using RSFCL as the additional support along with conventional converter control strategy based on the PI controller to further increase the rated active power of the installation, thereby enhancing dc-link voltage smoothness as well as the LVRT capability of the 50 MW WPP. Moreover, that was demonstrated that RSFCL can be a promising solution for improving wind turbine controller performance with respect to extreme loads on the wind turbine structure. With this approach, it is expected that the activation of the dc braking chopper and fast pitch angle control could be reduced in order to meet the international grid code requirements. An important feature of the proposed method is that a conventional PI control can be used, performing the reactive and reactive current injection, while the dc-link voltage never exceeds its safety limits. A further study is carried out to determine optimal performance of the combinatorial 50 MW PMSG-WPP and RSFCL. Therefore, the simultaneous and transformative approach based on the AHP method for the multiobjective optimization of embedded system has been introduced. A reconciliation between the three objecting functions, namely, resistive of SFCL, output power of PMSG, and energy dissipated in RSFCL has elicited by a 3-D alignment in the Pareto front having nondominated 25 solutions. However, a designer would be capable of selecting any of the solutions setting on the Pareto front without erratic problems on optimality.

Acknowledgement

The authors would like to thank Ms. Bonnie Jonkman, the Senior Scientist of National Wind Technology Center (NWTC), National Renewable Energy Laboratory (NREL), for her critical and extensive support for using the FAST version 8.

Appendix A

Table 1
Limits of variables for optimization problem.

Symbol	Quantity	Value
P_{rated}	Critical Temperature for HTS tape	15
T_0	liquid nitrogen temperature	77 K
I_{co}	Critical current	5 kA
C_p	Specific heat of HTS	$3\text{ MJm}^{-3}\text{K}^{-1}$

Table 1 (continued)

Symbol	Quantity	Value
P_{cool}	Cooling power	700 kW
V_{SC}	HTS Volume	$3e-4\text{m}^3$
A_{SC}	HTS Cross section	$1e-6\text{m}^2$
R_{sh}	Shunt resistance of HTS	$120\ \Omega$
ρ_n	Normal resistivity	$4e-8\ \Omega\text{m}$
ρ_f	Flux flow resistivity	$1e-9\ \Omega\text{m}$

Table 2

Parameters of the proposed PMSG-WPP for simulation.

Symbol	Quantity	Value
Wind turbine parameters		
P_t	Rated turbine power	2 MW
v_{wind}	Rated wind speed	12 m/s
R	Blade radius	46 m
ρ	Air density	1.225 kg/m^3
C_{p-opt}	Optimal power coefficient	0.45
λ_{opt}	Optimal tip speed ratio	8.32
PMSG parameters		
P_{rated}	Rated generator power	2 MW
V_{rms}	Rated rms line-line voltage	0.69 kV
f	Rated frequency	60 Hz
ψ_r	Rated rotor flux	17 Wb
ω_m	Rated speed	1200 rpm
R_s	Stator winding resistance	0.015 pu
L_s	Stator winding inductance	0.057 pu
R_r	Rotor resistance	0.105 pu
L_d, L_q	d, q-axis synchronous inductance and q-axis	8.75 mH
P	Number of Poles	6
H	Mechanical time constant	2.5 s

Table 3

Limits of variables for optimization problem.

Symbol	Quantity	Min value	Step	Max value
V_{SC}	Volume of HTS	$5e-4\text{m}^3$	$5e-4\text{m}^3$	$1e-3\text{m}^3$
A_{SC}	Cross section of HTS	$1e-6\text{m}^2$	$5e-6\text{m}^2$	$1e-5\text{m}^2$
Δt_{sc}	Duration of the fault	0 s	0.2 s	1.8 s

References

- [1] S.M. Muyeen, R. Takahashi, T. Murata, J. Tamura, A variable speed wind turbine control strategy to meet wind farm grid code requirements, *IEEE Trans. Power Syst.* 25 (1) (2010) 331–340.
- [2] A. Moghadasi, A. Sarwat, J.M. Guerro, A comprehensive review of low-voltage-ride-through methods for fixed-speed wind power generators, *Renew. Sustain. Energy Rev.* 55 (2016) 823–839.
- [3] M. Mohseni, S.M. Islam, Review of international grid codes for wind power integration: diversity, technology and a case for global standard, *Renew. Sustain. Energy Rev.* 16 (6) (2012) 3876–3890.
- [4] A. Moghadasi, A. Islam, Enhancing LVRT capability of FSIG wind turbine using current source UPQC based on resistive SFCL, in: T&D Conference and Exposition, 2014 IEEE PES, 2014, pp. 14–17.
- [5] A. Moghadasi, A. Islam, Enhancing LVRT capability of FSIG wind turbine using current source UPQC based on resistive SFCL, *IET Gener. Transm. Distrib.* 8 (3) (2014) 563–572.
- [6] Z. Zhang, Y. Zhao, W. Qiao, L. Qu, A discrete-time direct torque control for direct-drive PMSG-based wind energy conversion systems, *Ind. Appl. IEEE Trans.* 51 (4) (July-Aug. 2015) 3504–3514.
- [7] K. Ki-Hong, J. Yoon, L. Dong, K. Heung, LVRT scheme of PMSG wind power systems based on feedback linearization, *IEEE Trans. Power Electron.* 27 (5) (2012) 2376–2384.

- [8] V. Yaramasu, Bin Wu, S. Alepuz, et al., Predictive control for low-voltage ride-through enhancement of three-level-boost and NPC-converter-based PMSG wind turbine, *IEEE Trans. Ind. Electron.* 61 (12) (2014) 6832–6843.
- [9] M. Farhadi, O. Mohammed, Event based protection scheme for a multi-terminal hybrid dc power system, *IEEE Trans. Smart Grid* 6 (4) (2015) 1658–1669.
- [10] G. Yonghao, K. Chunghun, C. Chung, Nonlinear control for PMSG wind turbine via port-controlled Hamiltonian system, in: PowerTech, 2015 IEEE Eindhoven, July 2015, pp. pp.1–6.
- [11] A. Mullane, G. Lightbody, R. Yacamini, Wind-turbine fault ride-through enhancement, *IEEE Trans. Power Syst.* 20 (4) (2005) 1929–1937.
- [12] S. Alepuz, A. Calle, S. Busquets, S. Kouro, Bin Wu, Use of stored energy in PMSG rotor inertia for low-voltage ride-through in back-to-back NPC converter-based wind power systems, *IEEE Trans. Ind. Electron.* 60 (5) (2013) 1787–1796.
- [13] R.A. Ibrahim, M.S. Hamad, Y.G. Dessouky, B.W. Williams, A novel topology for enhancing the low voltage ride through capability for grid connected wind turbine generators, in: Energy Conversion Congress and Exposition (ECCE), Raleigh, NC, Sept., 2012, pp. 2389–2395.
- [14] S.M. Muyeen, M.H. Ali, T. Murata, J. Tamura, Transient stability enhancement of wind generator by a new logical pitch controller, *IEEJ Trans. Power Energy* 126 (8) (2006) 742–752.
- [15] K. Amei, Y. Takayasu, T. Ohji, M. Sakui, A maximum power control of wind generator system using a permanent magnet synchronous generator and a boost chopper circuit, in: Proc. Power Convers. Conf., Osaka, Japan, 2002, pp. pp.1447–1452.
- [16] F. Luo, D.S. Ma, Design of digital tri-mode adaptive output buck-boost power convertor for high efficient integrated systems, *IEEE Trans. Ind. Electron.* 57 (6) (2010) 2151–2160.
- [17] M. Farhadi, O. Mohammed, Adaptive energy management in redundant hybrid dc microgrid for pulse load mitigation, *IEEE Trans. Smart Grid* 6 (1) (2015) 54–62.
- [18] M. Farhadi, O. Mohammed, Performance enhancement of actively controlled hybrid DC microgrid and pulsed power load, *IEEE Trans. Ind. Appl.* 51 (5) (2015) 3570–3578.
- [19] F. Deng, Z. Chen, Low-voltage ride-through of variable speed wind turbines with permanent magnet synchronous generator, in: Proc. IEEE IECON, Porto, Portugal, Nov. 2009, pp. 621–626.
- [20] A. Mullane, G. Lightbody, R. Yacamini, Wind-turbine fault ride-through enhancement, *IEEE Trans. Power Syst.* 20 (4) (2005) 1929–1937.
- [21] J. Matas, M. Castilla, et al., Feedback linearization of direct-drive synchronous wind-turbines via a sliding mode approach, *IEEE Trans. Power Electron.* 23 (3) (2008) 1093–1103.
- [22] M.E. Elshiekh, D.A. Mansour, A.M. Azmy, Improving fault ride-through capability of DFIG-based wind turbine using superconducting fault current limiter, *IEEE Trans. Appl. Supercond.* 23 (3) (2013) 1204–1208.
- [23] L. Ye, L. Lin, Study of superconducting fault current limiters for system integration of wind farms, *IEEE Trans. Appl. Supercond.* 20 (3) (2010) 1233–1237.
- [24] H. Heydari, A.H. Moghadasi, Optimization scheme in combinatorial UPQC and SFCL using normalized simulated annealing, *IEEE Trans. Power Deliv.* 26 (3) (2011) 1489–1498.
- [25] S.-Y. Kim, W.-W. Kim, J.-O. Kim, Determining the location of superconducting fault current limiter considering distribution reliability, *IET Gener. Transm. Distrib.* 6 (3) (2012) 240–246.
- [26] Vahid Vahidinasab, Optimal distributed energy resources planning in a competitive electricity market: multiobjective optimization and probabilistic design, *Renew. Energy* 66 (2015) 345–363.
- [27] A.H. Moghadasi, H. Heydari, M. Farhadi, Pareto optimality for the design of SMES solenoid coils verified by magnetic field analysis, *IEEE Trans. Appl. Supercond.* 21 (1) (2011) 13–20.
- [28] M. Rosyadi, S.M. Muyeen, R. Takahashi, J. Tamura, Low voltage ride-through capability improvement of wind farms using variable speed permanent magnet wind generator, in: Electrical Machines and Systems (ICEMS), Beijing, China, Aug. 2011, 1,6, 20–23.
- [29] F. Jaramillo, G. Kenne, F. Lamnabhi, A novel online training neural network-based algorithm for wind speed estimation and adaptive control of PMSG WT system for maximum power extraction, *Renew. Energy* 86 (2015) 38–48.
- [30] S.H. Hosseini, A. Farakhor, S.K. Haghhighian, Novel algorithm of maximum power point tracking (MPPT) for variable speed PMSG wind generation systems through model predictive control, in: Electrical and Electronics Engineering (ELECO), 8th International Conference, 2013, pp. pp.243–247.
- [31] J. Adhikari, I.V. Prasanna, S.K. Panda, Maximum power-point tracking of high altitude wind power generating system using optimal vector control technique, in: Power Electronics and Drive Systems (PEDS), IEEE 11th International Conference, 2015, pp. pp.773–778.
- [32] S. Hunping, J.L. Nilles, High-accuracy hysteretic current-mode regulator for powering microprocessors, in: Applied Power Electronics Conf. APE, Twenty-first Annual IEEE, March 2006, pp. 19–23.
- [33] T. Janowski, S. Kozak, et al., Analysis of transformer type superconducting fault current limiters, *IEEE Trans. Appl. Supercond.* 17 (2) (2007) 1788–1790.
- [34] A. Gyore, S. Semperger, et al., Experimental analysis of different type HTS rings in fault current limiter, *IEEE Trans. Appl. Supercond.* 17 (2) (2007) 1899–1902.
- [35] S.M. Blair, C.D. Booth, N.K. Singh, G.M. Burt, Analysis of energy dissipation in resistive superconducting fault-current limiters for optimal power system performance, *IEEE Trans. Appl. Supercond.* 21 (4) (2011) 3452–3457.
- [36] S. Eckroad, Superconducting Fault Current Limiters, Electrical Power Research Institute (EPRI), Technology Watch, 2009.
- [37] J. Mulholland, T. Sheahan, B. Mcconnel, Method for estimating future markets for high-temperature superconducting power devices, *IEEE Trans. Appl. Supercond.* 12 (2) (2002) 1784–1789.
- [38] NREL, NWTC Information Portal, <https://nwtc.nrel.gov/FAST>.
- [39] P. Odgaard, L. Larsen, R. Wisniewski, T. Hovgaard, On using Pareto optimality to tune a linear model predictive controller for wind turbines, *Renew. Energy* 87 (2016) 884–891.
- [40] H. Li, C. Yang, Y. Hu, X. Liao, Z. Zeng, C. Zhe, An improved reduced-order model of an electric pitch drive system for wind turbine control system design and simulation, *Renew. Energy* 93 (2016) 188–200.
- [41] H. Heydari, R. Sharifi, Three-dimensional pareto-optimal design of inductive superconducting fault current limiters, *IEEE Trans. Appl. Supercond.* 20 (5) (2010) 2301–2311.